

# Defect-Polymorphism-Controlled Electrophoretic Propulsion of Anisometric Microparticles in a Nematic Liquid Crystal

Devika V S,<sup>1</sup> Dinesh Kumar Sahu,<sup>1</sup> Ravi Kumar Pujala<sup>2</sup>, and Surajit Dhara<sup>1,\*</sup>

<sup>1</sup>*School of Physics, University of Hyderabad, Hyderabad 500046, India*

<sup>2</sup>*Soft and Active Matter Group, Department of Physics, Indian Institute of Science Education and Research (IISER), Tirupati, Andhra Pradesh 517507, India*



(Received 1 February 2022; revised 15 April 2022; accepted 13 May 2022; published 13 July 2022)

The nontrivial shape of colloidal particles creates complex elastic distortions and topological defects in liquid crystals and plays a key role in governing their electrophoretic propulsion through the medium. Here, we report experimental results on defects and the electrophoretic transport of anisometric (snowman-shaped) polystyrene particles subjected to an alternating electric field perpendicular to the director in a nematic liquid crystal. We demonstrate that the shape asymmetry gives rise to defect polymorphism by nucleating point or ring defects at multiple locations on the particle and controls the direction as well as the magnitude of the electrophoretic propulsion. Unlike spherical particles, quadrupolar anisometric particles can be transported in multiple directions in the plane perpendicular to the applied field. Our findings provide an alternative degree of freedom in translocating microparticles in liquid crystals for applications in microfluidics, controlled transport, and directed assembly.

DOI: 10.1103/PhysRevApplied.18.014030

## I. INTRODUCTION

Active control of microparticles and fluids at the microscale by transducing the energy of an external electric field has been a subject of intense study owing to its wide applications, ranging from directed assembly of colloids to sorting of macromolecules, biomolecules, and microfluidics [1–6]. In an isotropic suspension (e.g., aqueous) particles are propelled due to the classical (linear) or the induced-charge electrophoresis (ICEP) [7–11]. In classical electrophoresis, charged colloidal particles move with a velocity,  $v \propto E$  as a result of field-induced electroosmotic flow of the counter ion cloud screening them. However, when it comes to ICEP, transport occurs due to the symmetry breaking of electrohydrodynamic flows (EHD) on the surface of a polarizable particle, and the particle moves with a velocity,  $v \propto E^2$  [11]. Such systems are often used as a synthetic model for living microswimmers, thus providing opportunities for developing tactic active matter [12].

In liquid crystals (LCs), the mechanism is markedly different from their isotropic counterparts as the particles distort the medium, and break the symmetry of near-field (local) director (average direction of molecular orientation) by nucleating topological defects [13,14]. A spherical particle with homeotropic surface anchoring in a nematic liquid crystal (NLC) nucleates either a point defect known

as hyperbolic hedgehog (strength,  $m = -1$ ) or a disclination ring defect ( $m = -1/2$ ) called Saturn ring [15–17]. The particles, accompanying point or ring defects, are known as elastic dipoles or quadrupoles, respectively, in analogy with electrostatics [13,14].

The applied electric field in NLCs creates a spatial charge separation across particles in the distorted regions with a charge density  $\rho$  proportional to the strength of the electric field  $E$ . In response, an electrostatic force,  $f \propto \rho E \sim E^2$  starts acting on the induced space-charge cloud around them. This force drives the LC molecules surrounding the particles, a phenomenon known as LC-enabled electro-osmosis (LCEO) [18–20]. For spherical dipolar particles, the fore-aft symmetry of LCEO flow is broken due to the asymmetric director configuration; as a result they propel along the far-field director  $\hat{n}$ . Whereas, in the case of quadrupolar particles the fore-aft symmetry of LCEO flow is preserved and hence they do not propel [21,22], except for metal-dielectric Janus particles reported recently [23–25].

While the transport of spherical particles in NLCs has been extensively investigated, recent advances in colloidal synthesis as well as the advent of three-dimensional (3D) printing have made it possible to fabricate microparticles with complex geometries [26–30]. It is known that the shape asymmetry of particles play an important role in inducing a variety of defects, complex assemblies [31–39], as well as transport in NLCs [40–43]. For example, reconfigurable swarms of shape anisometric particles could be

\* surajit@uohyd.ac.in

assembled and transported collectively in NLC, which is a significant step towards realizing fluid based lab-on-a chip technologies [40]. However, controlling the electrokinetics by modulating defects around the particle in NLCs is as yet unexplored. In this paper, we report experimental studies on defects and electrokinetics of snowman-shaped particles in an NLC. We show that unlike spherically symmetric particles, the point or ring defects are stabilized at multiple locations on the snowman particles. Such morphology-dependent defect polymorphism gives rise to rich electrokinetic phenomena, which provides the opportunity to control the magnitude as well as the direction of motion of these particles.

## II. EXPERIMENT

### A. Sample and cell preparation

We work with anisometric polystyrene microparticles, obtained from Magsphere Inc. (USA). Their shape resembles a snowman (SM) with two lobes having different diameters,  $D_1 = 3.0 \mu\text{m}$  and  $D_2 = 1.6 \mu\text{m}$ , and a center-to-center separation  $L = 1.5 \mu\text{m}$ . The separation factor, defined as  $2L/(D_1 + D_2)$  [28], is 0.69 in our case, which is less than their dimeric form, where  $2L/(D_1 + D_2) = 1$ . The surface of the SM particles is coated with a thin (50-nm) layer of  $\text{SiO}_2$ , following a method discussed later.

Further, the particles are coated with *N,N*-dimethyl-*N*-octadecyl-3 aminopropyltrimethoxysilyl chloride (known as DMOAP), which provides normal or homeotropic anchoring of LC molecules. A room-temperature nematic liquid crystal (MJ 98468, Merck), having birefringence  $\Delta n = 0.077$  is used in the experiment. In the low-frequency regime ( $< 200 \text{ Hz}$ ), it exhibits negative dielectric anisotropy and positive conductivity anisotropy (Appendix, Fig. 8). A small quantity (approximately equal to 0.01 wt%) of DMOAP-coated SM particles is dispersed in the nematic phase through vortex mixing and sonication. The experimental cells are made of two indium-tin-oxide-(ITO) coated glass plates. The plates are spin coated with a polyimide AL-1254 (JSR Corporation, Japan), cured at  $180^\circ\text{C}$ , and then rubbed unidirectionally using a benchtop rubbing machine (HO-IAD-BTR-01) to obtain a planar alignment of the nematic director,  $\hat{\mathbf{n}}$ . Two such plates are assembled, similar to the parallel-plate capacitor configuration [see Fig. 2(a)], and fixed with a UV curable adhesive mixed with spherical glass beads (diameter  $8 \mu\text{m}$ ). The actual cell gap is measured through an interferometric technique. Electrical contacts to the cells are provided by soldering two thin and flexible wires onto the ITO substrates.

### B. Procedure for silica coating

Initially, 3 g of polymer polyvinylpyrrolidone (PVP,  $40 \text{ kg mol}^{-1}$ ) is added to 30 ml of 1-pentanol and sonicated

for 2 h. Then,  $200 \mu\text{l}$  of polystyrene particles is added to the above solution and dispersed homogeneously after which, 3 ml of ethanol,  $840 \mu\text{l}$  of milli-Q water and  $200 \mu\text{l}$  of 0.18-M sodium citrate dihydrate are added to the dispersion and shaken thoroughly for 3 min. In the next step,  $675 \mu\text{l}$  of ammonia solution (25 wt%) is added to it. After 5 min,  $500 \mu\text{l}$  of tetraethoxysilane (TEOS) is added to the mixture and shaken gently for 3 min. The reaction is continued for 15 min. Immediately after 15 min, the particles are washed a few times with ethanol to obtain silica-coated snowman particles.

### C. Experimental setup

We use an inverted polarizing optical microscope (Nikon eclipse Ti-U) with a  $60\times$  water-immersion objective (Nikon, NIR Apo 60/1.0). A first-order full-wave retardation plate or  $\lambda$  plate (530 nm) is employed for constructing the director profile surrounding the SM particles. A function generator (AFG 3102, Tektronix) connected to a voltage amplifier (TEGAM 2350) is used for applying ac electric field. A CCD video camera (iDs-UI) attached to the microscope is used to record the particle trajectories at frame rates of 20–100 per second. A particle tracking program is used offline to track the position of particles. A Fiji Imagej plugin Trackmate is used for creating color-coded trajectories of particles [44].

## III. RESULTS AND DISCUSSION

Snowman-shaped particles coated with DMOAP mostly orient with their long axis parallel to the far-field director  $\hat{\mathbf{n}}$ , enforced by the rubbing direction. A fraction of them (Appendix, Fig. 7) are also oriented at different angles with respect to the rubbing direction, which is discussed later. The particles oriented parallel to the rubbing direction spontaneously induce dipolar- or quadrupolar-type director configurations. However, in sharp contrast to spherical particles, they show defect polymorphism in which the point and ring defects nucleate either on the big or small lobe of the snowman as shown in Figs. 1(c), 1(f), 1(i), and 1(l). The near-field director distortions and resulting defects are elucidated by inserting a full-wave retardation plate or  $\lambda$  plate between the crossed polarizers [Figs. 1(d), 1(g), 1(j), and 1(m)]. Two types of dipolar configurations are identified based on the position of point defects. For type-I dipoles, the point defect is nucleated on the small lobe [Fig. 1(e)], whereas, for type-II dipoles the point defect is nucleated on the big lobe [Fig. 1(h)]. Similarly, two quadrupolar-type defect structures are observed depending on whether the Saturn ring is present on the small (type-I) or big (type-II) lobe of the particle as shown schematically in Figs. 1(k) and 1(n).

For simplicity, we present all these particles sequentially in a progressive manner such that the transformation from one to another defect along the length of the particle is

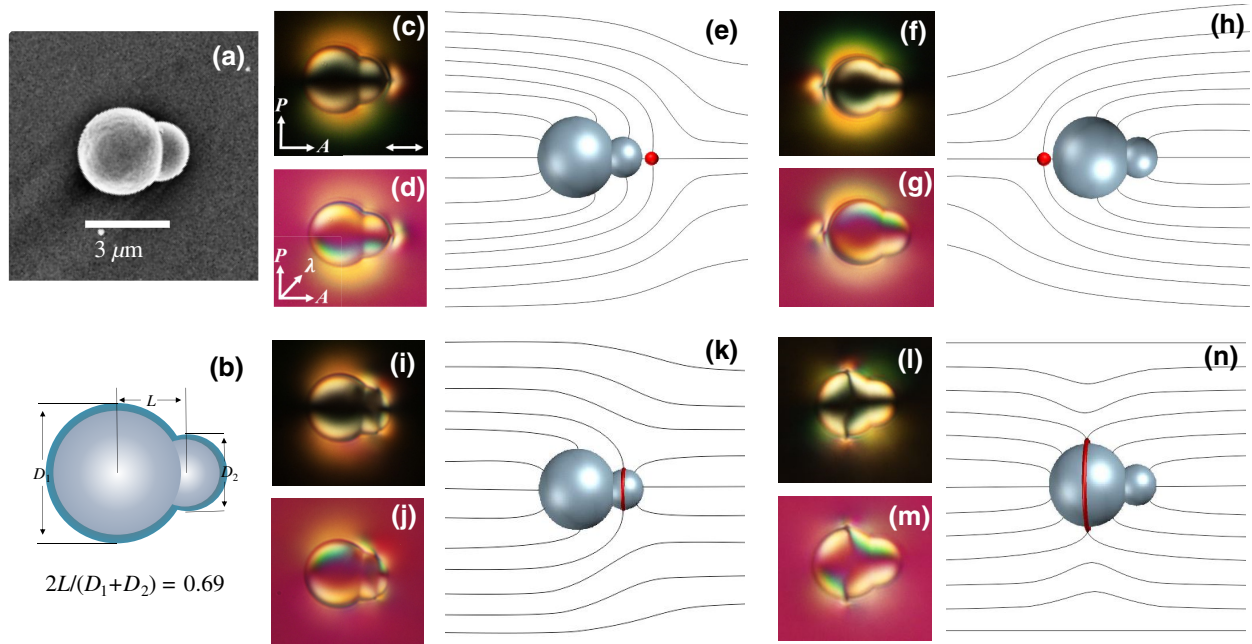


FIG. 1. (a) SEM image of a SM particle. (b) Cross section of the core-shell structure of a particle. Thickness of the silica shell (cyan) is 50 nm. Separation factor  $2L/(D_1 + D_2) = 0.69$ . Polarizing optical microscope (POM) images of SM particles in NLC with (c) point defect on the small lobe, (f) point defect on the big lobe, (i) Saturn ring defect on the small lobe, and (l) Saturn ring defect on the big lobe. (d),(g),(j),(m) Corresponding images taken by inserting a  $\lambda$  plate (530 nm) with slow axis at an angle of  $45^\circ$  between the sample and analyser. (e),(h),(k),(n) Schematic of director profiles around the particles. Red dot and red circles represent point and Saturn ring defects. Double-headed arrow represents the nematic director.  $P, A$  represents polarizer and analyzer.

topologically permitted in a continuous manner [Fig. 4(a)]. Starting from the left, the point defect is nucleated on the small lobe [Fig. 4(a)(i)], then it slightly opens up to form a Saturn ring encircling the small lobe [Fig. 4(a)(ii)], which then migrates to form a larger ring encircling the big lobe [Fig. 4(a)(iii)]. Finally, the larger ring collapses on the left side of the big lobe and transforms to a point defect [Fig. 4(a)(iv)]. Such polymorphism in defects is allowed as a ring defect of strength,  $m = -1/2$  is topologically equivalent to a hyperbolic hedgehog defect of strength,  $m = -1$ . In effect, the shape asymmetry of SM particles gives rise to rich defect polymorphism, which is absent in symmetric particles. Sometimes, we also use a dynamic laser tweezers' setup for controlling the position of defects or transforming dipoles to quadrupoles or vice versa by a photothermal quenching method [16,46].

We study the electrokinetics of SM particles under square-wave electric field  $\mathbf{E}$  (frequency range 10–100 Hz), applied perpendicular to the director as shown in Fig. 2(a). The electric field does not affect the macroscopic director  $\hat{\mathbf{n}}$  as the dielectric anisotropy ( $\Delta\epsilon$ ) of the liquid crystal MJ-98468 is negative in the working frequency range (Appendix, Fig. 8). First, we consider type-I and type-II dipolar SM particles only. Beyond a threshold electric field, both the particles start propelling parallel to the far-field director  $\hat{\mathbf{n}}$  as shown in Figs. 2(c) and 2(d) (see

Movies S1, S2 within the Supplemental Material [45]). Here, we define a vector  $\hat{\mathbf{s}}$  (directed towards the center of the small lobe from the center of the big lobe), which indicates the shape polarity of the particle [Fig. 2(b)]. For type-I dipolar particles, the point defect on the small lobe leads the way, and the propelling direction is parallel to  $\hat{\mathbf{s}}$  as shown in Fig. 2(c) (particle moving from right to left). Whereas, for type-II dipolar particles, the point defect on the big lobe leads the motion and the propelling direction is opposite to  $\hat{\mathbf{s}}$  as shown in Fig. 2(d) (particle moving from left to right). The electrophoretic velocity of a spherical particle of radius  $R$  is given by [21]

$$u = \alpha \frac{\epsilon_0 \bar{\epsilon} R}{\eta} \left( \frac{\Delta\epsilon}{\bar{\epsilon}} - \frac{\Delta\sigma}{\bar{\sigma}} \right) E^2, \quad (1)$$

where  $\alpha$  is a constant,  $\eta$  is the viscosity,  $\bar{\epsilon} = (\epsilon_{||} + \epsilon_{\perp})/2$  is the average dielectric permittivity, and  $\bar{\sigma} = (\sigma_{||} + \sigma_{\perp})/2$  is the average conductivity of the LC medium. Usually the sign of the term  $(\Delta\epsilon/\bar{\epsilon} - \Delta\sigma/\bar{\sigma})$  decides the direction of motion of the dipolar particles. If it is negative, the point defect leads the way and if it is positive the point defect trails behind the trajectory [47]. For our liquid crystal (MJ-98468) this quantity is negative ( $-1.5$ ) in the working frequency range, hence the point defect leads the motion

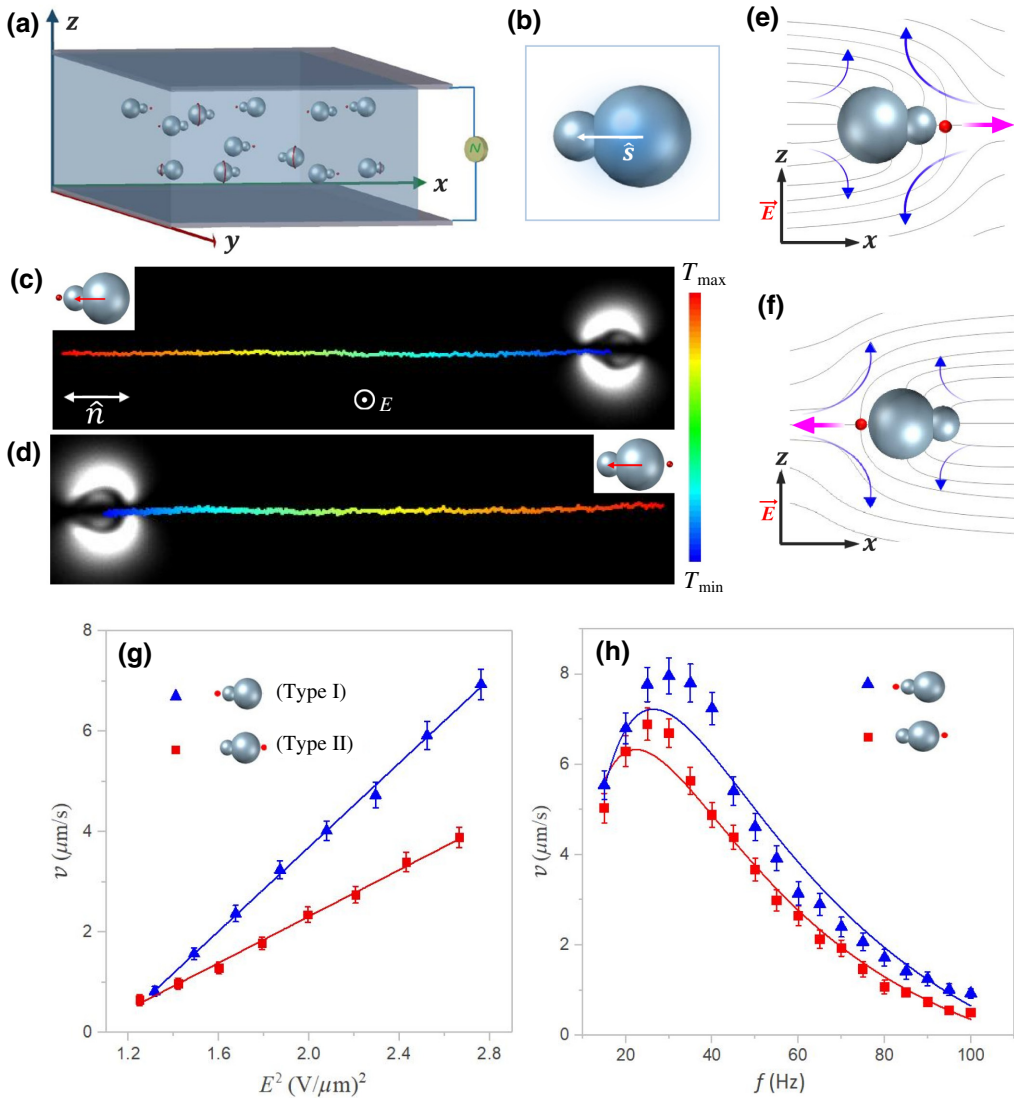


FIG. 2. (a) SM particles in a planar cell with an ac field along the  $z$  axis. Director  $\hat{\mathbf{n}}$  is parallel to the  $x$  axis. (b) Defining polar vector  $\hat{\mathbf{s}}$ . (c),(d) Time-coded trajectories of propulsion of type-I and type-II dipolar SM particles (see Movies S1 and S2 within the Supplemental Material [45]).  $T_{\min} = 0$  s and  $T_{\max} = 20$  s. Applied field  $E = 1.3 \text{ V}/\mu\text{m}$  at 50 Hz. Double-headed arrow represents the director  $\hat{\mathbf{n}}$ . (e),(f) LCEO flows (puller type) marked by blue curved arrows. Magenta-colored arrows indicate propulsion direction. (g) Field-dependent velocity of type-I and type-II dipolar SM particles. Blue (red) line represents least-squares fits to Eq. (1) for type-I (type-II) particles with slopes  $4.18$  and  $2.3 \mu\text{m}^3 \text{ V}^{-2} \text{ s}^{-1}$ , respectively (h) Frequency dependence of velocity of type-I and type-II dipolar SM particles. Solid curves represent least-squares fits to Eq. (2). Error bar shows the standard deviation of the mean value.

as expected. An interesting feature of the transport of dipolar SM particles in NLC is that the direction of motion of the particles could be reversed without reversing the shape polarity vector  $\hat{\mathbf{s}}$ , in contrast to their response in aqueous suspensions [48,49].

The field-dependent velocities of type-I and type-II dipolar particles are notably different. Figure 2(g) shows that the velocities of both types of dipolar SM particles are proportional to  $E^2$ , as expected in LC-enabled electrophoresis (LCEEP). But, the slope of type-I dipoles is almost double that of type II, which means that at a given field, type-I dipoles propel with twice the velocity

of type-II dipoles. The mobility of dipolar spherical particles in NLCs is due to the breaking of fore-aft symmetry of the surrounding LCEO flow owing to the asymmetric director structure. For SM particles, the symmetry of the LCEO flow is broken due to the asymmetric director structure owing to the shape. Due to this combined effect, the type-I dipolar particles propel at higher velocities than type-II dipoles. In analogy with spherical particles [21], we schematically present LCEO flows around the dipolar SM particles in Figs. 2(e) and 2(f). The flow is pusher type with respect to the field for both types of dipoles, but the magnitude of the flow is stronger near the small

lobe for type I, whereas it is stronger near the big lobe for type-II dipoles. The stronger flows near the respective lobes of the type-I and type-II dipoles control their direction of transport. The effect of shape asymmetry is also reflected in the frequency-dependent velocity as shown in Fig. 2(h). The velocity of type-I dipolar particles is greater than that of the type-II dipoles at all frequencies and it can be approximately fitted to [9,22]

$$v(\omega) = v_0 \frac{\omega^2 \tau_e^2}{(1 + \omega^2 \tau_e^2)(1 + \omega^2 \tau_p^2)}, \quad (2)$$

where  $\omega = 2\pi f$ ,  $\tau_e$ , and  $\tau_p$  are the electrode and particle charging times that regulates the electro-osmotic flows surrounding the particles, and are related to the lower and upper limits of the driving frequencies. We obtain moderate fittings to Eq. (2) when compared to that of spherical particles [23]. It may be mentioned that in our system, both Reynolds number ( $Re \ll 1$ ) and Erickson number ( $Er \ll 1$ ) are very small; hence, the fluid inertia has no effect and the director configuration surrounding the motile particles remain unchanged. Also, the particles are away from the electrodes due to wall-dipole or quadrupole elastic repulsion, known as elastic levitation [50].

In what follows, we study the frequency-dependent velocity of dipolar particles (type I) at different electric fields. A comparison of frequency-dependent velocity profiles at three fields, with a stepwise increase ( $0.15 \text{ V}/\mu\text{m}$ ) from  $1.56$  to  $1.85 \text{ V}/\mu\text{m}$  is shown in Fig. 3(a). With increasing field the frequency profile becomes sharper, and

the peak frequency as well as the velocities rise to higher values. For example, the peak frequency is enhanced from  $30$  to  $60 \text{ Hz}$  and the velocity (at the peak) increases from  $7.5$  to  $22.2 \mu\text{m}/\text{s}$  when the field is increased from  $1.56$  to  $1.85 \text{ V}/\mu\text{m}$ . The total shift in the peak frequency of SM particles (approximately  $30 \text{ Hz}$ ) is much greater than that measured for spherical particles ( $f \sim 10 \text{ Hz}$ ) having similar size [Appendix, Fig. 9(b)]. We also fit the velocity profiles at higher fields to Eq. (2) and observe that a moderate fitting to the data can be obtained when  $\tau_e \approx \tau_p$  (Appendix, Table I). It is analogous to the situation of frequency-dependent electro-osmotic flows driven by ac fields at adjacent electrodes in microfluidic channels [10]. This suggests that at stronger fields the electro-osmotic flow between the electrodes dominates over the local flow surrounding the particles.

We further explore the low-frequency regime ( $<20 \text{ Hz}$ ) of the velocity profile of SM dipoles. The frequency-dependent velocity profile at  $E = 1.56 \text{ V}/\mu\text{m}$  [Fig. 3(a)] shows that the motion of the particle is stopped below  $15 \text{ Hz}$ . When the frequency is reduced nearly to  $10 \text{ Hz}$ , interestingly the SM particles start moving again but in the opposite direction of their earlier motion as shown in Figs. 3(b) and 3(c) (see Movie S5 within the Supplemental Material [45]). This unusual behavior of the particles at low frequencies points to an adept mechanism for direction reversal, which could otherwise be obtained only by changing the sign of the physical quantity ( $\Delta\epsilon/\bar{\epsilon} - \Delta\sigma/\bar{\sigma}$ ) [47]. It is confirmed that both the dielectric and conductivity anisotropies do not change

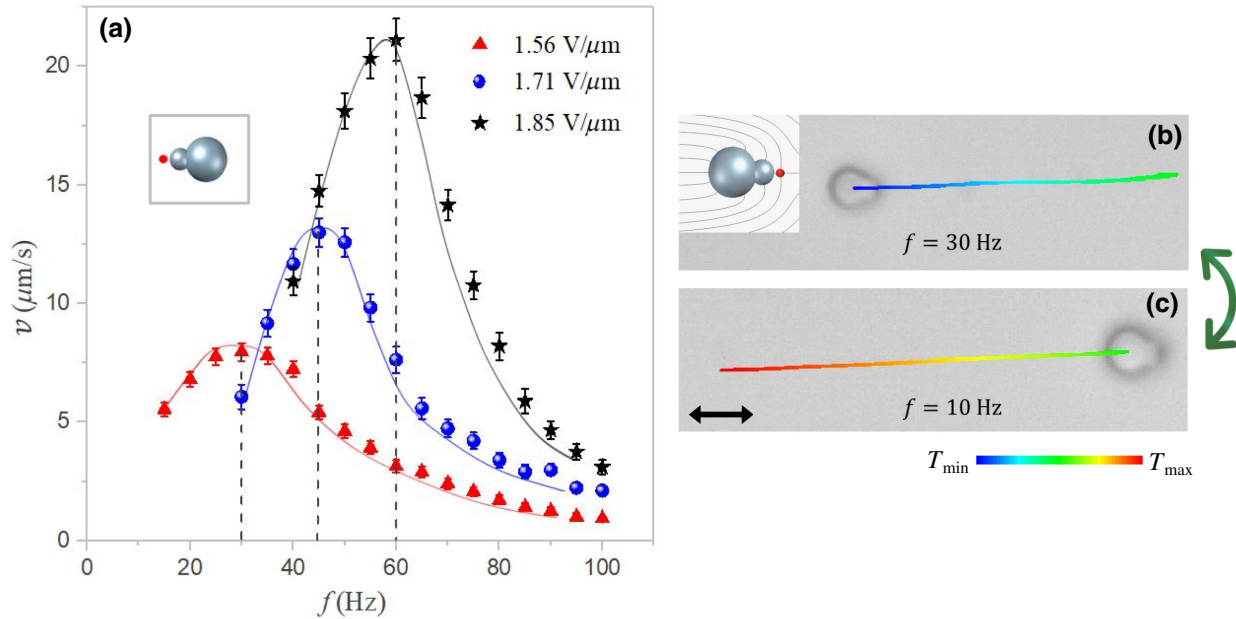


FIG. 3. (a) Frequency dependence of the electrophoretic velocity of SM dipolar particles at three different electric field values  $1.56$ ,  $1.71$ , and  $1.85 \text{ V}/\mu\text{m}$ . Solid curves are a guide to the eye. Vertical dotted lines indicate the frequencies corresponding to maximum velocities. (b),(c) Reversal of direction of motion from  $+\hat{s}$  to  $-\hat{s}$  by changing the frequency from  $30$  to  $10 \text{ Hz}$ , keeping the field constant at  $E = 1.3 \text{ V}/\mu\text{m}$  (see Movie S5 within the Supplemental Material [45]).  $T_{\min} = 0 \text{ s}$  and  $T_{\max} = 13 \text{ s}$ .

sign when the frequency is changed from 20 to 10 Hz ([Appendix](#), Fig. 8). In the low-frequency regime, particles can be transported due to the Carr-Helfrich instability [51,52] in which the nematic forms thin cylindrical vortices, perturbing the initial director orientation [53–55]. A careful observation through a high magnification objective (100 $\times$ ) revealed that no visible electroconvection (so-called Williams domains) occurred in the LC cell during the reverse motion of particles. This reversal in motion, however, is limited to a very narrow frequency range (10–7 Hz), below which the particle's movement becomes random due to visible electrohydrodynamic instabilities. This means that the direction reversal occurs just before the onset of the Carr-Helfrich instability. The same phenomenon is observed at other fields also, but at different frequencies.

At the onset of the instability, the external electric field tends to align the director along the  $z$  direction whereas, the elastic torque tries to restore its initial orientation. As a

result of these two competing torques, slight director distortion starts developing across the sample. This director reorientation in the vicinity of the hedgehog, which is still intact, induces a current flow  $\mathbf{J}$  along the director ( $x$  direction), leading to charge accumulation [56]. In response, an additional local field  $\mathbf{E}(x)$  develops along the  $x$  direction. Migration of charges under  $\mathbf{E}(x)$  creates a local flow, which we anticipate is the reason that causes the particles to propel in the opposite direction.

Next, we study the electrokinetics of type-I (Saturn ring on small lobe) and type-II (Saturn ring on big lobe) quadrupolar SM particles. The direction of the electric field is the same as shown in Fig. 2(a). Unlike spherical quadrupoles, which are immobile, type-I and type-II SM quadrupolar particles propel parallel to the director  $\hat{\mathbf{n}}$ . Figures 4(b)(ii,iii) present the time-coded trajectories of type-I and type-II quadrupolar SM particles. We also include the results of type-I and type-II dipolar SM particles for a comparative discussion and greater insight. SM

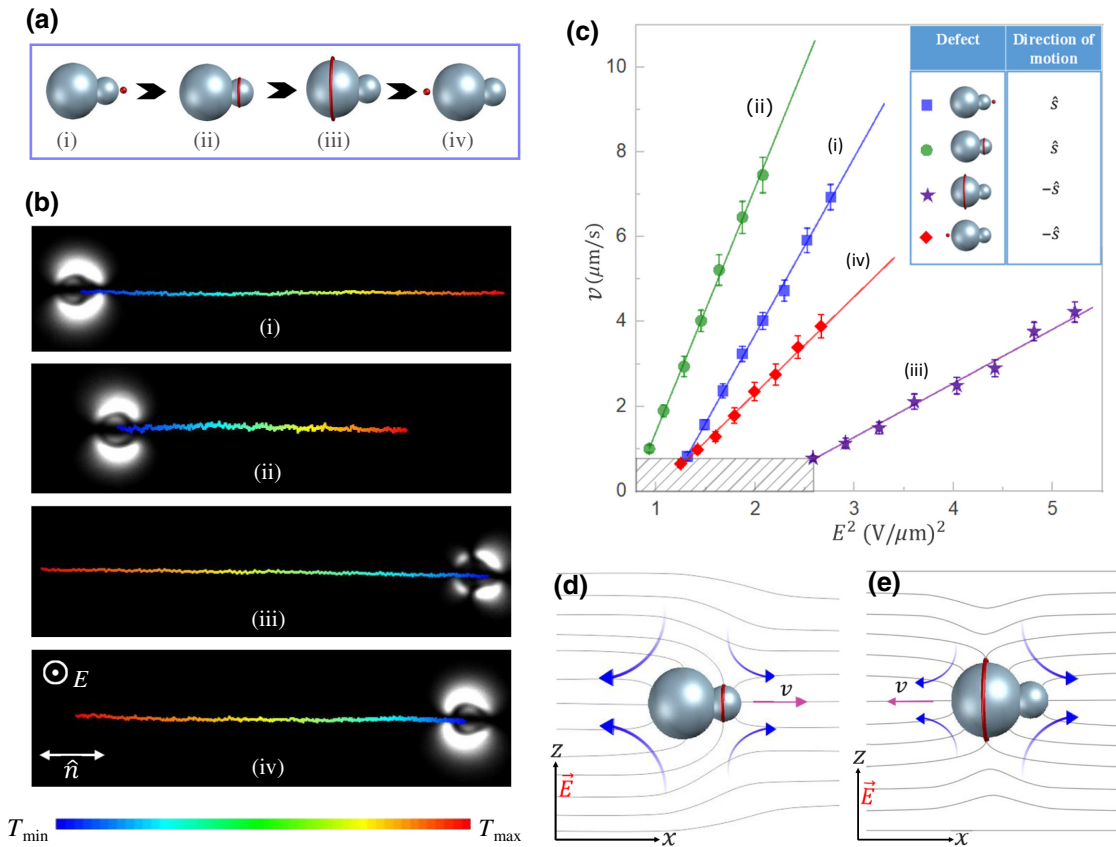


FIG. 4. (a) Arrangement of particles showing the progression of defects (left to right) from a point defect on the small lobe to a point defect on the big lobe through two successive ring-defects. (b) Time-coded trajectories of the particles as labelled from (i) to (iv). Note that particles with point and ring defects (Movies S1 and S2 [45]) on small lobe propel from right to left and particles with point and ring defects on big lobe (Movies S3 and S4 [45]) propel from left to right ( $T_{\min} = 0$  s to  $T_{\max} = 20$  s). (c) Variation of velocities at a fixed frequency 50 Hz of four particles as a function of  $E^2$  with slopes (i)  $4.18 \mu\text{m}^3 \text{V}^{-2} \text{s}^{-1}$ , (ii)  $5.76 \mu\text{m}^3 \text{V}^{-2} \text{s}^{-1}$ , (iii)  $1.27 \mu\text{m}^3 \text{V}^{-2} \text{s}^{-1}$ , and (iv)  $2.28 \mu\text{m}^3 \text{V}^{-2} \text{s}^{-1}$ . Inset shows the direction of motion of respective particles either parallel or antiparallel to  $\hat{s}$ . No electrophoretic transport is observed below the threshold fields (shaded region). LCEO flow fields in the  $xz$ -plane around (d) type-I and (e) type-II quadrupolar SM particles.

particles with point or ring defects on the small lobe propel along the same direction (right to left) with the direction of motion parallel to  $\hat{s}$  [Fig. 4(b)(i,ii)]. This is because the ring defect on the small lobe creates elastic distortions somewhat similar to dipolar particles as evident from the two-lobe pattern observed under cross polarizers.

SM particles with point or ring defects on the big lobe propel with the direction of motion antiparallel to  $\hat{s}$  [Fig. 4(b)(iii,iv)]. It should be noted that in contrast to spherical particles, the four-lobe pattern of type-II SM quadrupoles is asymmetric [Fig. 4(b)(iii)]. Apart from direction, the magnitude of the electrophoretic velocities of

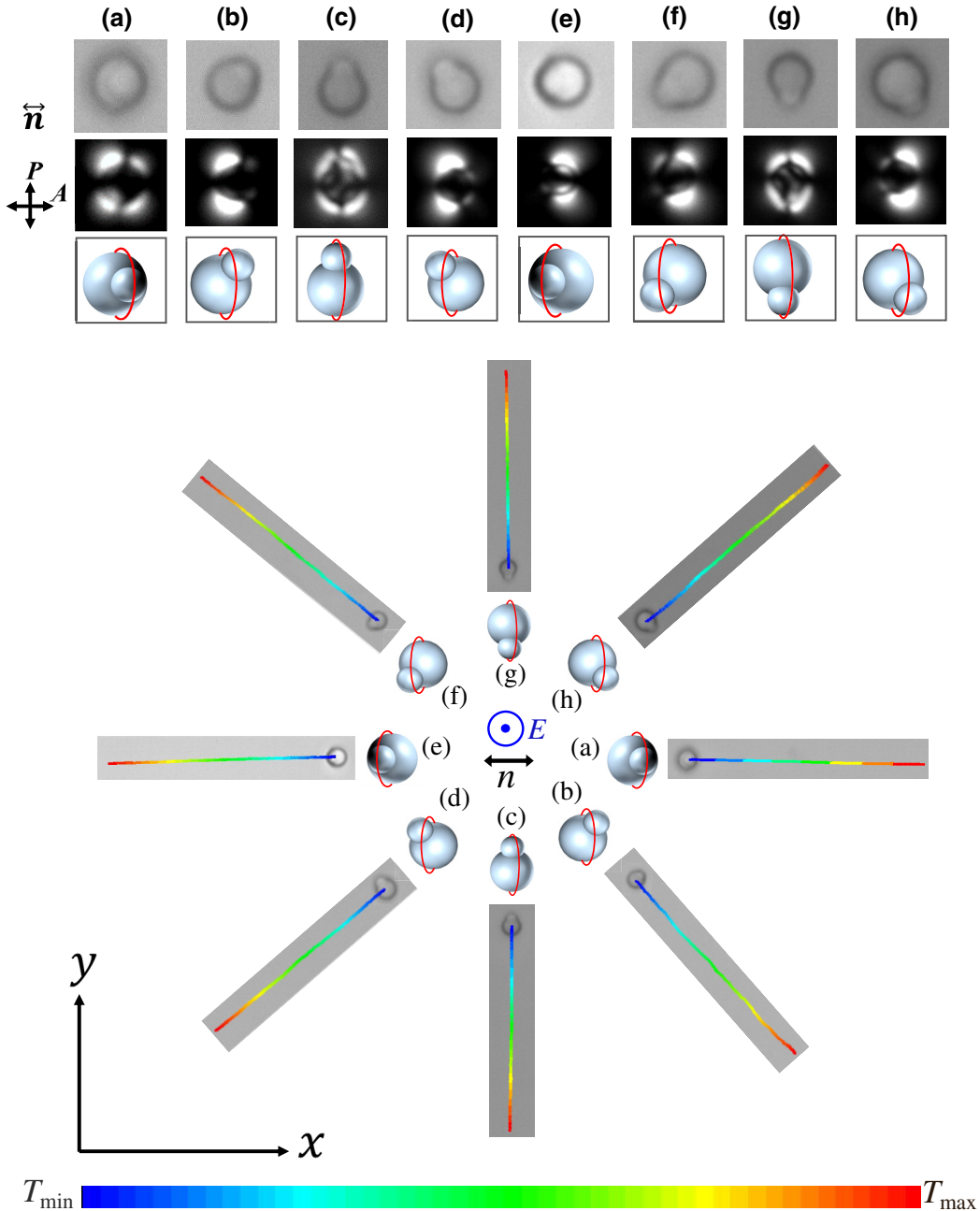


FIG. 5. (a)–(h) CCD images (first row), corresponding POM images (second row) and schematics (third row) of a few SM quadrupolar particles. All particles, except (c) and (g) are tilted along the vertical direction. (i) Time-coded trajectory of the particles under ac electric field ( $T_{\min} = 0$  s to  $T_{\max} = 10$  s).  $f = 30$  Hz and field range, 1–1.5 V/ $\mu$ m. Trajectories of the particles are grouped to demonstrate omnidirectional transport. The direction of the electric field and the director  $\hat{n}$  for all trajectories are shown in the center. Cell thickness, 8  $\mu$ m (see Movie S6 within the Supplemental Material [45]).

the SM particles are also significantly different. Figure 4(c) shows the variation of velocities of all four defect types mentioned above. It varies quadratically with field, but with different slopes for each defect configuration. For a given field, type-I quadrupoles move with velocity almost one order of magnitude higher than type-II quadrupoles [comparing Fig. 4(c)(ii) and (iii)]. A comparative analysis of different defect types reveals the fact that, for a given field, a wide range of transport velocities could be achieved by tailoring the defects accompanying the particles. Thus, defect polymorphism of the SM particles leads to manifold transport in terms of direction as well as magnitude.

As mentioned earlier, spherical quadrupolar particles do not propel due to the fore-aft symmetry of the LCEO flow. In our case, the quadrupolar symmetry of the director field [Figs. 1(k) and 1(n)] and hence, the fore-aft symmetry of the LCEO flow is broken due to the inherent shape asymmetry of the particles. The transport of such particles can be explained in details based on the electrostatic force density. The force density acting on a spherical quadrupolar particle (with ring defect) with the electric field  $E_0\hat{z}$  applied perpendicular to the far-field director ( $x$  axis) can be written as [23]

$$\mathcal{F} \simeq \epsilon_0(-\Delta\epsilon + \Delta\sigma G_\epsilon^{-1}G_\sigma)\left[\frac{\partial\theta}{\partial z}\frac{\partial\Psi_0}{\partial x} + \frac{\partial\theta}{\partial x}\frac{\partial\Psi_0}{\partial z}\right]E_0\hat{z}, \quad (3)$$

where  $G_\sigma = (\sigma_\perp\nabla_\perp^2 + \sigma_\parallel\nabla_\parallel^2)^{-1}$ ,  $G_\epsilon = (\epsilon_\perp\nabla_\perp^2 + \epsilon_\parallel\nabla_\parallel^2)^{-1}$  are positive operators and  $\Psi_0$  represents the electrostatic potential due to the applied electric field and  $\theta$  is the angle of the near-field director with respect to the rubbing direction. For LCs with  $\Delta\epsilon < 0$  and  $\Delta\sigma > 0$ , the force dipole and resulting flow directions around the particle is determined by the quantity in the square brackets. The director

curvatures in Eq. (3) are composed of a bend component concentrated just outside the Saturn ring ( $\partial_x\theta$ ) coupled to ( $\partial_z\Psi_0$ ) and a splay component on the particle surface ( $\partial_z\theta$ ) coupled to ( $\partial_x\Psi_0$ ). It has been shown that pure splay contribution gives rise to a force dipole of contractile or puller type, while pure bend contribution produces a force dipole of pusher type with respect to the direction of electric field [23]. In our case of quadrupolar SM particles (type I and type II), the symmetry breaking in the  $x$ - $z$  plane is of relevance, where the splay component dominates and hence generates a puller-type flow pattern [Figs. 4(d) and 4(e)]. The symmetry of this flow is broken due to asymmetric director field induced by the particles. It is expected that the flow is stronger on the surface of big lobe when the ring defect resides on the small lobe, due to its relatively large splay contribution. Similarly the strength of the flow is more on the surface of the small lobe when the ring defect shifts to the big lobe. Thus depending on the position of the ring defect, particles can move either parallel or antiparallel to  $\hat{s}$  (forward or backward) as shown in Figs. 4(d) and 4(e).

So far, we discuss the defects and transport of SM particles whose shape polarity vector ( $\hat{s}$ ) is oriented along the rubbing direction. Next, we look at quadrupolar SM particles whose  $\hat{s}$  is tilted (in the plane or out of the plane) with respect to the director ( $\hat{n}$ ). The first row of Fig. 5 [i.e., from (a) to (h)] shows examples of a few particles. The polarity vector  $\hat{s}$  of the particles shown in Figs. 5(c) and 5(g) are perpendicular to the rubbing direction, and for the rest  $\hat{s}$  is tilted out of the plane at different angles. The corresponding elastic deformations under crossed polarizers and the schematic of the defects are shown in the second and third rows, respectively. It is evident from the POM images that the anisometric shape of the particle induces asymmetric elastic distortions in all cases, without exception.

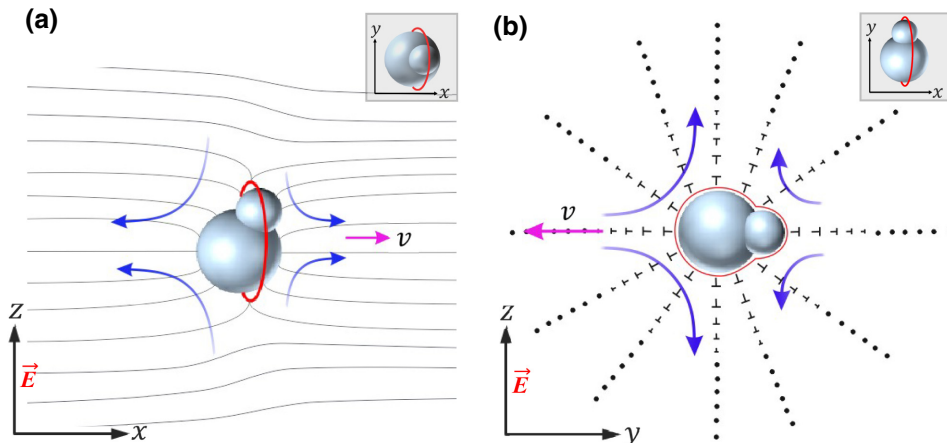


FIG. 6. (a) Liquid-crystal-enabled electro-osmotic flows around a quadrupolar SM particle in two orthogonal planes parallel to the electric field. The elastic distortion in the  $xz$ -plane is splay dominated, and  $yz$ -plane is bend dominated and the flow fields are (a) puller and (b) pusher with respect to the field. Red curves denote ring defects. The big blue arrows indicate stronger flow. The propulsion direction is indicated by a pink arrow.

Figure 5 presents a consolidated picture of various trajectories of tilted quadrupolar particles. Depending on the tilt, they are transported in different directions in the plane of the sample. For example, particles with only out-of-plane tilt (rotation) as shown in Figs. 5(a) and 5(e), which are mirror images about the  $z$  axis, propel along  $+x$  and  $-x$  directions, respectively. Here, the symmetry breaking of LCEO flow in the  $z$ - $x$  plane is of relevance, where the flow is of puller type (dominated by splay deformation). As shown in Fig. 6(a), the tilting of the particle breaks the flow symmetry around the ring defect and hence it propels along the  $+x$  direction. The motion of particle “e” can also be explained in a similar way. Particles with only in-plane tilt as shown in Figs. 5(c) and 5(g), which are mirror images about  $x$  axis, propel along  $+y$  and  $-y$  directions, respectively. Here, symmetry breaking occurs in the  $y$ - $z$  plane where the bend distortion dominates, hence the flow is of pusher type with respect to field as shown in Fig. 6(b). Again, due to shape asymmetry the fore-aft symmetry of this flow is broken, and as a result the particles propel along  $+y$  or  $-y$  direction.

Finally, we discuss the transport of quadrupolar SM particles having both in-plane and out-of-plane tilts as shown in Figs. 5(b), 5(d), 5(f) and 5(h). For such particles, the symmetry of the flow is broken in two orthogonal planes ( $x$ - $z$  and  $y$ - $z$ ). Consequently, they move at an angle with respect to the director, depending on the tilt. For instance, the shape polarity vector  $\hat{s}$  in Fig. 5(f) makes an angle of nearly  $50^\circ$  with the director in the  $x$ - $y$  plane, and also has an out-of-plane tilt. As we can see, the trajectory makes nearly  $40^\circ$  with the director, so that it is almost perpendicular to the shape polarity vector. Similarly, the trajectories of the remaining cases Figs. 5(b), 5(d), and 5(h) can also be explained.

#### IV. CONCLUSION

To summarize, snowman-shaped particles with homeotropic anchoring orient along the director or tilt at an angle to it, and induce point or ring defects at different locations. Specifically, a point or ring defect is nucleated either on the small or big lobe of SM particles oriented with their shape polarity vector parallel to the director. For particles with ring defects encircling either lobes, the quadrupolar symmetry of the director field is broken and they propel along the director with the direction of motion either parallel or antiparallel to the shape-polarity vector  $\hat{s}$ . Particles with point defect on the small lobe propel almost 2 times faster than the particles with point defect on the big lobe. Such shape-dependent defect polymorphism results in reversible electrophoretic transport with varied magnitudes in velocities. We also observe a frequency-dependent reversal of propulsion direction of dipolar particles at the onset of low-frequency electrohydrodynamic instabilities. In effect, we have at our disposal two tangible mechanisms for reversing

the direction of transport of the particles without altering the sign of the dielectric and conductivity anisotropies of the medium. The defect-guided manifold elecrokinetics demonstrated here is in sharp contrast to that which are known for spherically symmetric particles. We demonstrate omnidirectional transport of quadrupolar particles in which the symmetry of surrounding electro-osmotic flows is broken due to shape as well as tilting with respect to the director. Our findings uncover alternative possibilities of controlling electrophoretic transport of particles in multiple directions at will, which makes them useful candidates for applications like targeted delivery at the microscale. Evidently, particles with customised shape are promising candidates for achieving diversity in electrokinetic motility for applications in micro robotics, microfluidics, and lab-on-a chip devices. The alternative particle steering strategy demonstrated in this work can be extended as well for liquid inclusions for controlled chemical reactions in the microscale. Moreover, we can envisage an extension of our strategy to living systems by employing biocompatible lyotropic liquid crystals.

#### ACKNOWLEDGMENTS

S.D. gratefully acknowledges the support from the DST (DST/SJF/PSA-02/2014-2015), and University of Hyderabad (UoH/IoE/RC1- 20-010). D.V.S. and D.K.S. acknowledge DST for INSPIRE fellowship. R.K.P. acknowledges the Department of Science and Technology for INSPIRE Faculty Award Grant [DST/INSPIRE/04/2016/002370] and a Grant (CRG/2020/006281, DST-SERB), Government of India, for funding.

#### APPENDIX

Figure 7 shows the relative population of the different defects. Percentage of particles with point defect on the smaller lobe is much larger than the particles with point defect on the big lobe. The relative population of particles with ring defects depends on the cell gap [Fig. 7(b)]. In thicker cells ( $13\ \mu\text{m}$ ), the number of particles with

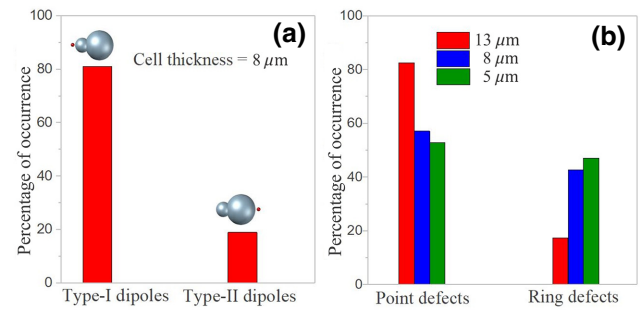


FIG. 7. (a) Relative population of dipolar particles with point defect on small and big lobes. (b) Relative population of particles with point and ring defects in different cell thicknesses.

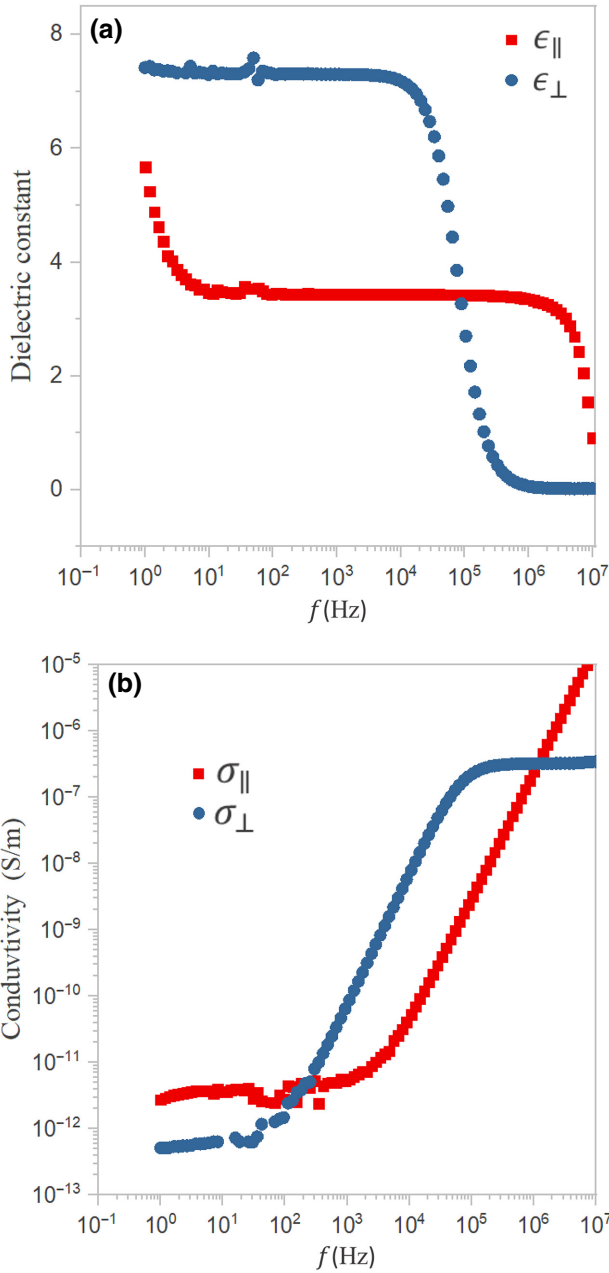


FIG. 8. Frequency-dependent parallel and perpendicular components of (a) dielectric constant and (b) conductivity of MJ-98468. Parallel components ( $\epsilon_{\parallel}$  and  $\sigma_{\parallel}$ ) are measured in homeotropic cells with the applied field parallel to the nematic director. Perpendicular components ( $\epsilon_{\perp}$  and  $\sigma_{\perp}$ ) are measured in homogeneous or planar cells with the applied field perpendicular to the nematic director.

point defect is more than the number of particles with ring defects as the cell gap is several times higher than the diameters of both lobes. However, in thinner cells ( $5 \mu\text{m}$ ), the number of particles with point and ring defects are almost equal as expected since the cell gap is comparable to diameters of the lobes.

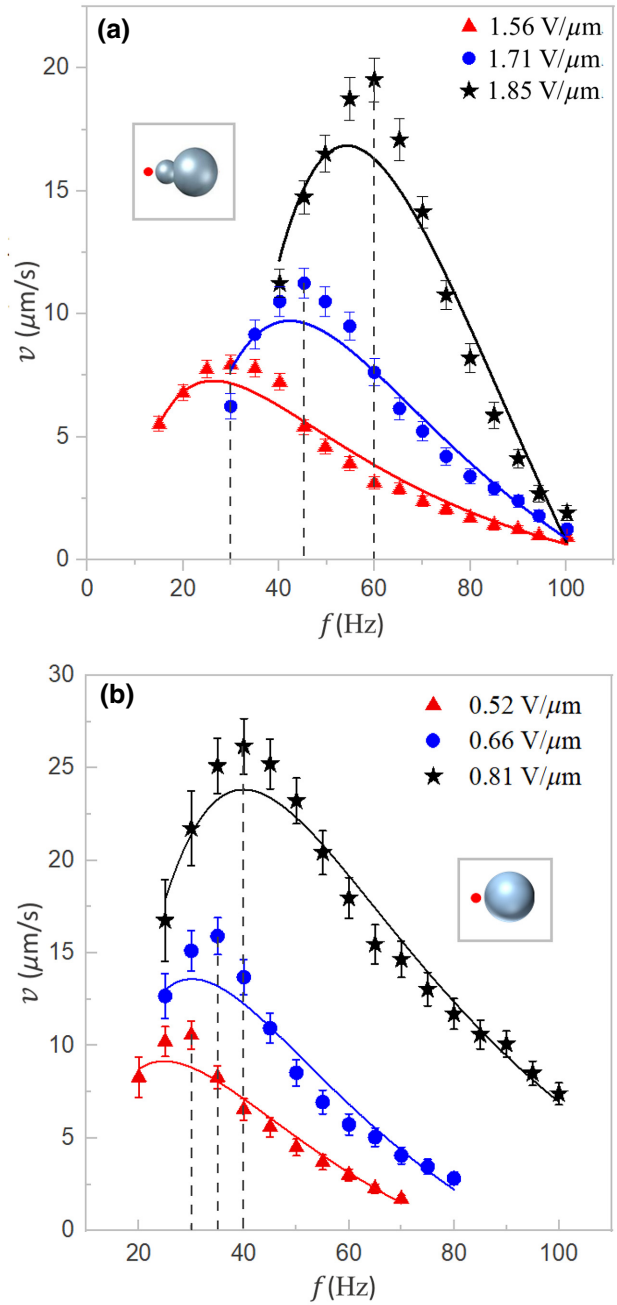


FIG. 9. Frequency-dependent velocity profile measured at three different fields of (a) dipolar SM particle, (b) dipolar silica microsphere of diameter  $3.0 \mu\text{m}$ . Solid curves are the best fit to Eq. (2). The total frequency shift for SM particle is about 30 Hz whereas for spherical particle it is about 10 Hz. The field ranges for the two particles are different but the difference between the highest and the lowest fields for both particles is almost the same, approximately 0.29 V/ $\mu\text{m}$ . The fit parameters are given in Table I.

We measure parallel ( $\epsilon_{\parallel}, \sigma_{\parallel}$ ) and perpendicular ( $\epsilon_{\perp}, \sigma_{\perp}$ ) components of the dielectric constant and conductivity at room temperature as a function of frequency using a dielectric spectrometer (Alpha-A Novocontrol) (Fig. 8).

TABLE I. Parameters obtained from fitting velocity profiles of dipolar SM particle and dipolar spherical particles to Eq. (2) at different electric fields.

Fit parameters	Dipolar spherical silica particles			Dipolar snowman particles		
	Electric field			Electric field		
	0.52 (V/ $\mu$ m)	0.66 (V/ $\mu$ m)	0.81 (V/ $\mu$ m)	1.56 (V/ $\mu$ m)	1.71 (V/ $\mu$ m)	1.85 (V/ $\mu$ m)
$\tau_e$ (s)	0.0873	0.058	0.033	0.08	0.024	0.018
$\tau_p$ (s)	0.0186	0.019	0.019	0.018	0.024	0.018

The parallel component is measured in a homeotropic cell and the perpendicular component is measured in a planar cell. In both cells the applied voltage is 0.1 V, which is much below the Freedericksz threshold value. In the frequency range of our experiments (15–100 Hz) the dielectric anisotropy is negative [Fig. 8(a)] and the conductivity anisotropy is positive [Fig. 8(b)]. For example, the values at 50 Hz are  $\Delta\epsilon = \epsilon_{||} - \epsilon_{\perp} = -3.9$  and  $\Delta\sigma = \sigma_{||} - \sigma_{\perp} \simeq 1.5 \times 10^{-11}$  S/m. The sign of both the anisotropies is changed at much higher frequency.

Figure 9(a) shows fittings of the velocity profile of SM dipolar particles to Eq. (2). The profile at field 1.56 V/ $\mu$ m fits reasonably well with fit parameters  $\tau_e = 0.08$  s and  $\tau_p = 0.18$  s, respectively. We obtain moderate fittings of the velocity response at higher fields when  $\tau_e \approx \tau_p$  (see Table I). For comparison we also measure frequency-dependent velocity of spherical silica particles as presented in Fig. 9(b). The peak frequency is shifted by about 10 Hz when the field is increased from 0.52 to 0.81 V/ $\mu$ m. The velocity profiles can be fitted reasonably well to Eq. (2). The fit parameters are presented in Table I.

electrokinetics at large applied voltages in concentrated solutions, *Adv. Colloid Interface Sci.* **152**, 48 (2009).

- [10] T. M. Squires and M. Z. Bazant, Induced-charge electroosmosis, *J. Fluid Mech.* **509**, 217 (2004).
- [11] M. Z. Bazant and T. M. Squires, Induced-Charge Electrokinetic Phenomena: Theory and Microfluidic Applications, *Phys. Rev. Lett.* **92**, 066101 (2004).
- [12] L. Alvarez, M. A. Fernandez-Rodriguez, A. Alegria, S. Arrese-Igor, K. Zhao, M. Kröger, and Lucio Isa, Reconfigurable artificial microswimmers with internal feedback, *Nat. Commun.* **12**, 4762 (2021).
- [13] P. Poulin, H. Stark, T. C. Lubensky, and D. A. Weitz, Novel colloidal interactions in anisotropic fluids, *Science* **275**, 1770 (1997).
- [14] H. Stark, Physics of colloidal dispersions in nematic liquid crystals, *Phys. Rep.* **351**, 387 (2001).
- [15] I. Mušević, M. Skarabot, U. Tkalec, M. Ravnik, and S. Žumer, Two-dimensional nematic colloidal crystals self-assembled by topological defects, *Science* **313**, 954 (2006).
- [16] I. Mušević, *Liquid Crystal Colloids* (Springer International Publishing AG, Cham, Switzerland, 2017).
- [17] I. I. Smalyukh, Liquid crystal colloids, *Annu. Rev. Condens. Matt. Phys.* **9**, 207 (2018).
- [18] O. D. Lavrentovich, Active colloids in liquid crystals, *Curr. Opin. Colloid Interface Sci.* **21**, 97 (2016).
- [19] O. D. Lavrentovich, Transport of particles in liquid crystals, *Soft Matter* **10**, 1264 (2014).
- [20] I. Lazo and O. D. Lavrentovich, Liquid-crystal-enabled electrophoresis of spheres in a nematic medium with negative dielectric anisotropy, *Phil. Trans. Soc. A* **371**, 2012255 (2013).
- [21] I. Lazo, C. Peng, J. Xiang, S. V. Shiyanovskii, and O. D. Lavrentovich, Liquid crystal-enabled electro-osmosis through spatial charge separation in distorted regions as a novel mechanism of electrokinetics, *Nat. Commun.* **5**, 5033 (2014).
- [22] O. D. Lavrentovich, I. Lazo, and O. P. Pishnyak, Nonlinear electrophoresis of dielectric and metal spheres in a nematic liquid crystal, *Nature* **467**, 947 (2010).
- [23] D. K. Sahu, S. Kole, S. Ramaswamy, and S. Dhara, Omnidirectional transport and navigation of Janus particles through a nematic liquid crystal film, *Phys. Rev. Res.* **2**, 032009(R) (2020).
- [24] D. K. Sahu and S. Dhara, Measuring Electric-Field-Induced Dipole Moments of Metal-Dielectric Janus Particles in a Nematic Liquid Crystal, *Phys. Rev. Appl.* **14**, 034004 (2020).

- [1] H. Morgan and N. G. Green, *AC Electrokinetics: Colloids and Nanoparticles* (Research Studies Press Ltd, Baldock, Hertfordshire, England, 2003).
- [2] A. Ramos, *Electrokinetics and Electrohydrodynamics in Microsystems* (Springer, Vienna, 2011).
- [3] S. V. Dorp, U. F. Keyser, N. H. Dekker, C. Dekker, and S. G. Lemay, Origin of the electrophoretic force on DNA in solid-state nanopores, *Nat. Phys.* **5**, 347 (2009).
- [4] A. Terray, J. Oakey, and D. W. M. Marr, Microfluidic control using colloidal devices, *Science* **296**, 1841 (2002).
- [5] A. F. Demirörs, F. Eichenseher, M. J. Loessner, and A. R. Studart, Colloidal shuttles for programmable cargo transport, *Nat. Commun.* **8**, 1872 (2017).
- [6] R. C. Hayward, D. A. Saville, and I. A. Aksay, Electrophoretic assembly of colloidal crystals with optically tunable micropatterns, *Nature* **404**, 56 (2000).
- [7] V. A. Murtsovkin, Nonlinear flows near polarized disperse particles, *Colloid J.* **58**, 341 (1996).
- [8] T. M. Squires and S. R. Quake, Microfluidics: Fluid physics at the nanolitre scale, *Rev. Mod. Phys.* **77**, 977 (2005).
- [9] M. Z. Bazant, M. S. Kilic, B. D. Storey, and A. Ajdari, Towards an understanding of induced-charge

- [25] D. K. Sahu and S. Dhara, Electric field driven controllable motility of metal-dielectric Janus particles with boojum defects in thin films of a nematic liquid crystal, *Phys. Fluids* **33**, 0187106 (2021).
- [26] S. Sacanna and D. J. Pine, Shape-anisotropic colloids: Building blocks for complex assemblies, *Curr. Opin. Colloid Interface Sci.* **16**, 96 (2011).
- [27] S. Sacanna, M. Korpics, K. Rodriguez, L. Colón-Meléndez, S.-H. Kim, D. J. Pine, and Gi-Ra Yi, Shaping colloids for self-assembly, *Nat. Commun.* **4**, 1688 (2013).
- [28] M. Liu, F. Dong, N. S. Jackson, M. D. Ward, and M. Weck, Customized chiral colloids, *J. Am. Chem. Soc.* **142**, 16528 (2020).
- [29] C. Zhu, A. J. Pascall, N. Dudukovic, M. A. Worsley, J. D. Kuntz, E. B. Duoss, and C. M. Spadaccini, Colloidal materials for 3D printing, *Annu. Rev. Chem. Biomol. Eng.* **10**, 17 (2019).
- [30] R. A. Archer, J. R. Howse, S. Fujii, H. Kawashima, G. A. Buxton, and S. J. Ebbens, pH-Responsive catalytic Janus motors with autonomous navigation and cargo-release functions, *Adv. Funct. Mater.* **30**, 2000324 (2020).
- [31] C. Lapointe, T. G. Mason, and I. I. Smalyukh, Shape-controlled colloidal interactions in nematic liquid crystals, *Science* **326**, 1083 (2009).
- [32] J. Dontabhaktuni, M. Ravnik, and S. Zumer, Quasicrystalline tilings with nematic colloidal platelets, *Proc. Natl. Acad. Sci. USA* **111**, 2464 (2014).
- [33] B. Senyuk, M. C. M. Varney, J. A. Lopez, S. Wang, N. Wu, and I. I. Smalyukh, Magnetically responsive gourd-shaped colloidal particles in cholesteric liquid crystals, *Soft Matter* **10**, 6014 (2014).
- [34] D. Andrienko, M. P. Allen, G. Skačej, and S. Žumer, Defect structures and torque on an elongated colloidal particle immersed in a liquid crystal host, *Phys. Rev. E* **65**, 041702 (2002).
- [35] C. P. Lapointe, K. Mayoral, and T. G. Mason, Star colloids in nematic liquid crystals, *Soft Matter* **9**, 7843 (2013).
- [36] M. V. Rasna, K. P. Zuhail, U. V. Ramudu, R. Chandrasekar, J. Dontabhaktuni, and S. Dhara, Orientation, interaction and laser assisted self-assembly of organic single-crystal micro-sheets in a nematic liquid crystal, *Soft Matter* **11**, 7674 (2015).
- [37] B. Senyuk, Q. Liu, S. He, R. D. Kamien, R. B. Kusner, T. C. Lubensky, and I. I. Smalyukh, Topological colloids, *Nature (London)* **493**, 200 (2013).
- [38] M. A. Gharbi, M. Cavallaro, G. Wu, D. A. Beller, R. D. Kamien, S. Yang, and K. J. Stebe, Microbullet assembly: Interactions of oriented dipoles in confined nematic liquid crystal, *Liq. Cryst.* **40**, 1619 (2013).
- [39] Rasi M. Muhammed, R. K. Pujala, and S. Dhara, Colloidal analogues of polymer chains, ribbons and 2D crystals employing orientations and interactions of nano-rods dispersed in a nematic liquid crystal, *Sci. Rep.* **9**, 4652 (2019).
- [40] S. Hernández-Navarro, P. Tierno, J. A. Farrera, J. Ignés-Mullol, and F. Sagués, Reconfigurable swarms of nematic colloids controlled by photoactivated surface patterns, *Angew. Chem. Int. Ed.* **53**, 10696 (2014).
- [41] A. V. Straube, J. M. Pagés, P. Tierno, J. Ignés-Mullol, and F. Sagués, Collective dynamics and conformal ordering in electrophoretically driven nematic colloids, *Phys. Rev. Res.* **1**, 022008(R) (2019).
- [42] A. V. Straube, J. M. Pagés, A. O. Ambriz, P. Tierno, J. Ignés-Mullol, and F. Sagués, Assembly and transport of nematic colloidal swarms above photo-patterned defects and surfaces, *New J. Phys.* **20**, 075006 (2018).
- [43] M. V. Rasna, U. V. Ramudu, R. Chandrasekar, and S. Dhara, Propelling and spinning of microsheets in nematic liquid crystals driven by ac electric field, *Phys. Rev. E* **95**, 012710 (2017).
- [44] D. Ershov, M. Phan, J. W. Pylyväinen, S. U. Rigaud, L. Le Blanc, A. Charles-Orszag, J. R. W. Conway, R. F. Laine, N. H. Roy, D. Bonazzi, G. Dumenil, G. Jacquemet, and J. Tinevez, BioRxiv:2021.09.03.458852.
- [45] See Supplemental Material at <http://link.aps.org/supplemental/10.1103/PhysRevApplied.18.014030> for movies.
- [46] K. P. Zuhail, M. Humar, and S. Dhara, Effect of phase transitions on liquid crystal colloids: A short review, *Liq. Cryst. Rev.* **8**, 44 (2021).
- [47] S. Paladugu, C. Conklin, J. Vinals, and O. D. Lavrentovich, Nonlinear Electrophoresis of Colloids Controlled by Anisotropic Conductivity and Permittivity of Liquid-Crystalline Electrolyte, *Phys. Rev. Appl.* **7**, 034033 (2017).
- [48] F. Ma, X. Yang, H. Zhao, and N. Wu, Inducing Propulsion of Colloidal Dimers by Breaking the Symmetry in Electrohydrodynamic Flow, *Phys. Rev. Lett.* **115**, 208302 (2015).
- [49] F. Ma, S. Wang, D. T. Wu, and N. Wu, Electric-field-induced assembly and propulsion of chiral colloidal clusters, *Proc. Natl. Acad. Sci. USA* **112**, 6307 (2015).
- [50] O. P. Pishnyak, S. Tang, J. R. Kelly, S. V. Shiyanovskii, and O. D. Lavrentovich, Levitation, Lift, and Bidirectional Motion of Colloidal Particles in an Electrically Driven Nematic Liquid Crystal, *Phys. Rev. Lett.* **99**, 127802 (2007).
- [51] P. G. de Gennes, *The Physics of Liquid Crystals* (Clarendon, Oxford, 1993).
- [52] L. M. Blinov, Electrohydrodynamic effects in liquid crystals, *Sci. Prog. Oxf.* **70**, 263 (1986).
- [53] Y. Sasaki, Y. Takikawa, V. S. R. Jampani, H. Hoshikawa, T. Seto, C. Bahr, S. Herminghaus, Y. Hidakac, and H. Orihara, Colloidal caterpillars for cargo transportation, *Soft Matter* **10**, 8813 (2014).
- [54] Y. Nishioka, F. Kobayashi, N. Sakurai, Y. Sasaki, and H. Orihara, Microscopic characterisation of self-assembled colloidal particles in electrohydrodynamic convection of a low-birefringence nematic liquid crystal, *Liq. Cryst.* **43**, 427 (2016).
- [55] K. Takahashi and Y. Kimura, Dynamics of colloidal particles in electrohydrodynamic convection of nematic liquid crystal, *Phys. Rev. E* **90**, 012502 (2014).
- [56] G. R. Acharya, PhD Thesis, Electroconvection and Pattern Formation in Nematic Liquid Crystal (2009).